SPECTROSCOPIC CHARACTERIZATION, DFT CALCULATION, AND DOCKING ANALYSIS FOR UNDERSTANDING MOLECULAR INTERACTION MECHANISM OF PROPICONAZOLE AND DNA

Neslihan Kaya Kinaytürk

Burdur Mehmet Akif Ersoy University, Faculty of Arts and Sciences, Department of Nanoscience and Nanotechnology, Burdur, Turkey; e-mail: nkinayturk@mehmetakif.edu.tr

This research presents a theoretical analysis based on structural and spectral data to elucidate the molecular interaction mechanism of propiconazole, a fungicide. The optimization, vibration bands, and electronic structure analysis were conducted using the B3LYP level density functional theory with the aug-cc-pVDZ basis set. Additionally, molecular docking simulations were performed to uncover the mechanism and modes of interaction between the propiconazole pesticide and DNA (PDB ID: 1BNA). The investigation revealed that the compound exhibits reactivity and polarizability, as indicated by the HOMO-LUMO energy range. The analysis of the molecular electrostatic potential surface (MEPS) and electrostatic potential surface (ESPS) demonstrated that the N6 and N7 atoms possess negative potential and serve as active sites for nucleophilic attacks. Similar observations were made for the oxygen and chlorine atoms. The molecular docking analysis indicated a preference for the propiconazole ligand to bind to DNA at sites involving nitrogen, oxygen, and chlorine atoms, specifically with guanine (G)-cytosine (C) interactions. Notably, the remarkable concordance between the MEP and molecular insertion results further supports these findings. These results provide valuable insights into the mechanism of DNA damage and the toxicological effects of the pesticide. Furthermore, the molecular docking analysis led to observations of changes in the optimized structure of the propiconazole molecule. For instance, the bond length between Cl1–C15, which was initially determined as 1.73 Å in the optimized structure, was recalculated as 1.77 Å following the molecular docking analysis.

Keywords: *propiconazole, density functional theory, molecular docking, molecular electrostatic potential surface, vibrational assignments.*

АНАЛИЗ ВЗАИМОДЕЙСТВИЯ ПРОПИКОНАЗОЛА С ДНК НА ОСНОВЕ РАСЧЕТОВ МЕТОДОМ ФУНКЦИОНАЛА ПЛОТНОСТИ И МОЛЕКУЛЯРНОГО ДОКИНГА

N. K. Kinaytürk

УДК 543.42

Университет Бурдура Мехмета Акифа Эрсоя,
Бурдур, Турция; e-mail: nkinayturk@mehmetakif.edu.tr

(Поступила 13 декабря 2022)

Теоретический анализ, основанный на структурных и спектральных данных, использован для выяснения механизма молекулярного взаимодействия пропиконазола — фунгицида — с ДНК. Оптимизация, анализ полос колебаний и электронной структуры проведены с использованием теории функционала плотности уровней B3LYP с базисным набором aug-cc-pVDZ. Проведено моделирование молекулярного докинга для определения механизма и способов взаимодействия между пестицидом пропиконазолом и ДНК (ID PDB: 1BNA). Показано, что соединение проявляет реакционную способность и поляризуемость, на что указывает диапазон энергий ВЗМО-НСМО. Анализ поверхности молекулярного электростатического потенциала (МЭП) и поверхности электростатического потен-

циала молекулы показал, что атомы N6 и N7 обладают отрицательным потенциалом и служат активными центрами для нуклеофильных атак. Аналогичные наблюдения сделаны для атомов кислорода и хлора. Анализ молекулярного докинга показал способность лиганда пропиконазола связываться с ДНК в сайтах, включающих в себя атомы азота, кислорода и хлора, в частности, с взаимодействиями гуанин (G)-цитозин (C). Соответствие результатов МЭП и молекулярной вставки подтверждает сделанные выводы. Результаты дают ценную информацию о механизме повреждения ДНК и токсикологическом воздействии пестицида. В результате анализа молекулярного докинга выявлены изменения в оптимизированной структуре молекулы пропиконазола. Длина связи Cl1–C15, которая изначально составляла 1.73 Å в оптимизированной структуре, пересчитана как 1.77 Å после анализа молекулярного докинга.

Ключевые слова: *пропиконазол, теория функционала плотности, молекулярный докинг, поверхность молекулярного электростатического потенциала, колебательные распределения.*

Introduction. Although the use of pesticides in agriculture brings significant economic benefits, their detrimental effects on the environment and human health cannot be overlooked [1–3]. Pesticide residues can accumulate in the human body through the food chain, biological enrichment, and environmental exposure [2]. Propiconazole, a broad-spectrum fungicide, is a triazole derivative developed by Janssen Pharmaceutics (Belgium) [4]. It is commonly applied to grasses, fruits, grains, seeds, hardwoods, and conifers [5, 6]. While propiconazole has demonstrated efficacy in combating various fungal attacks, prolonged use has been associated with toxic effects in mammals, fish, and certain invertebrates [7, 8] – for example, Pan et al. reported the stereoselective acute toxicity of propiconazole towards aquatic organisms such as Scenedesmus obliquus and Daphnia magna [8]. Wang et al. investigated the toxicity of propiconazole at the protein level and characterized its effects on human serum albumin (HSA) using molecular modeling and multi-spectroscopic methods [3]. In rats, the administration of propiconazole induced liver fibrosis through pathological changes, epithelial-mesenchymal transition, and collagen deposition [9]. Furthermore, exposure to propiconazole at concentrations typically used in agricultural fields significantly harmed flagellates [10]. These studies collectively demonstrate the serious toxic effects of propiconazole across a wide range of organisms, highlighting the need for further investigation into its characterization and interaction with DNA molecules.

Quantum chemical calculations are frequently employed to analyze the structural parameters, electronic properties frontier molecular orbital (FMO), Mullikan atomic charges, thermodynamic functions, and molecular electrostatic potential (MEP), as well as vibrational frequencies (IR and Raman) of diverse molecular systems. Density functional theory (DFT), an approach aimed at quantitatively comprehending material properties based on the fundamental principles of quantum mechanics, is a commonly preferred method for calculating the electronic structure of atoms and molecules [11]. DNA serves as the fundamental building block of life, carrying hereditary and genetic information through processes like replication and transcription. Given the significant importance of examining micro-molecule-DNA interactions and elucidating the interaction mechanisms, DNA is frequently chosen as the target molecule in studies involving various small molecules, including carcinogens [12].

Although numerous articles have been published on the toxicity and mechanisms of propiconazole, there has been a notable absence of studies characterizing propiconazole using the DFT method and investigating its interaction mechanism with DNA. We performed molecular modeling and spectroscopic characterization of propiconazole from a theoretical standpoint, and explored the propiconazole–DNA interaction using molecular docking. These calculations are of utmost importance as they provide essential insights into the molecular interaction mechanism of propiconazole, thereby enhancing our understanding at the molecular level.

Material and methods. The theoretical calculations in this study were conducted using the Gaussian 09 software package [13]. For the quantum chemical calculations, the DFT/B3LYP/aug-cc-pVDZ basis set was selected. Following the geometry optimization calculation, vibrational frequencies were obtained. It is well-known that B3LYP vibrational wavenumbers tend to be higher than experimental values. To align the theoretical values with the experimental ones, a uniform scaling factor of 0.9704 was applied. Theoretical data were visualized using the Gauss View program [14]. Additionally, the potential energy distributions of the observed vibration frequencies were calculated using the VEDA program [15]. For the molecular docking studies, Autodock Vina [16], Autodock Tools, and PyMOL Molecular Graphics System programs [17] were employed.

Results and discussion. Table 1 presents the optimized parameters, including bond lengths and bond angles, of the propiconazole molecular structure, with atom numbering as shown:

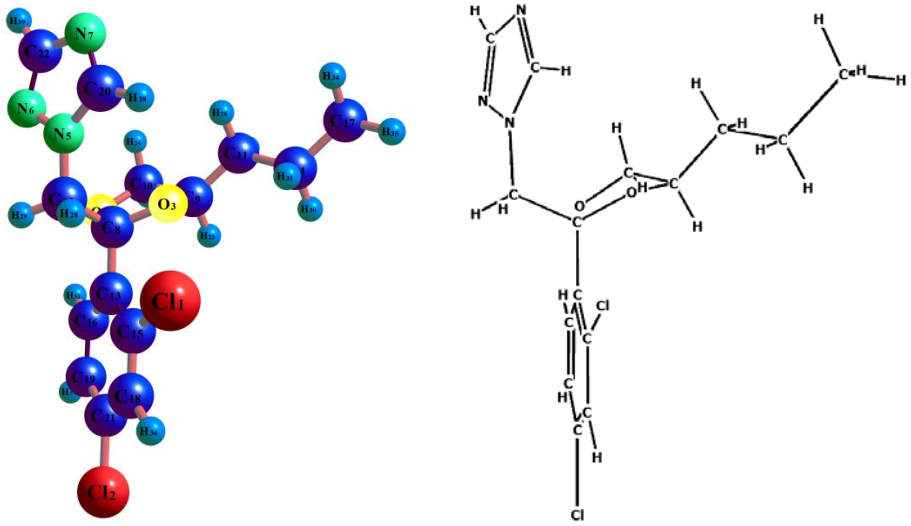

TABLE 1. Geometrical Parameters Optimized in Propiconazole, Bond Length *R* (*I*,*J*) and Bond Angles *A* (*I*,*J*,*K*)

Bond length, Å							
R(1,15)	1.73	*R*(7,22)	1.37	*R*(20,38)	1.08	*R*(16,32)	1.09
R(2,21)	1.72	*R*(8,12)	1.53	*R*(12,28)	1.10	*R*(17,33)	1.09
R(3,8)	1.44	*R*(8,13)	1.52	*R*(12,29)	1.10	*R*(17,34)	1.09
R(3,9)	1.43	*R*(9,10)	1.51	*R*(13,15)	1.40	*R*(17,35)	1.09
R(4,8)	1.44	*R*(9,11)	1.51	*R*(13,16)	1.40	*R*(18,21)	1.39
R(4,10)	1.43	*R*(9,23)	1.10	*R*(14,17)	1.52	*R*(18,36)	1.09
R(5,6)	1.33	*R*(10,24)	1.09	*R*(14,30)	1.10	*R*(19,21)	1.39
R(5,12)	1.46	*R*(10,25)	1.09	*R*(14,31)	1.10	*R*(19,37)	1.09
R(5,20)	1.35	*R*(11,14)	1.53	*R*(15,18)	1.40		
R(6,22)	1.33	*R*(11,26)	1.10	*R*(16,19)	1.39		
R(7,20)	1.31	*R*(11,27)	1.10	*R*(22,39)	1.08		
Bond angles, degree							
A(8,3,9)	104.96	*A*(5,20,38)	124.34	*A*(8,4,10)	105.34	*A*(4,10,25)	109.77
A(1,15,13)	121.18	*A*(7,20,38)	126.55	*A*(6,5,12)	120.25	*A*(9,10,24)	113.10
A(1,15,18)	118.73	*A*(2,21,18)	120.03	*A*(6,5,20)	112.39	*A*(9,10,25)	112.45
A(13,15,18)	120.09	*A*(2,21,19)	119.97	*A*(12,5,20)	127.37	*A*(24,10,25)	108.04
A(13,16,19)	120.11	*A*(18,21,19)	119.10	*A*(5,6,22)	100.32	*A*(9,11,14)	111.72
A(13,16,32)	121.54	*A*(6,22,7)	115.80	*A*(20,7,22)	102.38	*A*(9,11,26)	109.84
A(19,16,32)	118.35	*A*(6,22,39)	121.05	*A*(3,8,4)	108.62	*A*(9,11,27)	109.72
A(14,17,33)	110.98	*A*(7,22,39)	123.15	*A*(3,8,12)	107.85	*A*(14,11,26)	108.55
A(14,17,34)	110.10	*A*(8,3,9)	104.96	*A*(3,8,13)	110.85	*A*(14,11,27)	109.42
A(14,17,35)	110.28	*A*(26,11,27)	107.49	*A*(4,8,12)	108.57	*A*(11,14,31)	110.17
A(33,17,34)	108.31	*A*(5,12,8)	112.20	*A*(4,8,13)	110.48	*A*(8,13,15)	121.76
A(33,17,35)	108.08	*A*(5,12,28)	106.35	*A*(12,8,13)	110.40	*A*(8,13,16)	118.45
A(34,17,35)	108.09	*A*(5,12,29)	106.55	*A*(3,9,10)	102.73	*A*(15,13,16)	119.80
A(15,18,21)	120.00	*A*(8,12,28)	111.79	*A*(3,9,11)	110.59	*A*(11,14,17)	111.72
A(15,18,36)	120.10	*A*(8,12,29)	111.67	*A*(3,9,23)	107.71	*A*(11,14,30)	109.82
A(21,18,36)	119.90	*A*(28,12,29)	107.95	*A*(10,9,11)	114.01	*A*(4,10,25)	109.77
A(16,19,21)	120.01	*A*(5,20,7)	109.11	*A*(10,9,23)	110.35	*A*(9,10,24)	113.10
A(16,19,37)	119.21	*A*(4,10,24)	110.26	*A*(11,9,23)	110.98	*A*(9,10,25)	112.45
A(21,19,37)	120.78	*A*(4,10,9)	103.15	*A*(24,10,25)	108.04		

The calculated bond lengths for various atom pairs in propiconazole are as follows: Cl1-C15 (1.72 Å), Cl2-C21 (1.73 Å), N5-N6 (1.33 Å), N7-C20 (1.31 Å), N7-C22 (1.37 Å), N5-C20 (1.35 Å), and N6-C22 (1.33 Å). In a crystal structure study by Jin-Xiang and Chun-long [18], the experimental bond lengths were reported as follows: Cl-C (1.74 and 1.75 Å), N-C (1.44, 1.31, and 1.33 Å), N-N (1.36 Å), and C-O (1.39 and 1.42 Å). The bond lengths C8-O3 and C8-O4 were calculated as 1.44 Å.

Among the bond angles in propiconazole, the widest angle was observed between C12-N5-C20, calculated as 127.37°, which aligns with the experimental value of 128.8° reported in the study [18]. The bond angles between N5-N6-C12 and C20-N7-C22 were determined as 100.32 and 102.38°, respectively, which represent the smallest bond angles in the propiconazole molecule. The experimental values for these angles were reported as 102.5 and 102°, respectively. Overall, the theoretical calculations closely match the experimental data [18].

Propiconazole is composed of 39 atoms and exhibits 111 different types of vibrational modes. In this study, the vibrational modes were calculated using the DFT/B3LYP/aug-cc-pVDZ basis set. Specifically, propiconazole has 38 stretching modes, 37 bending modes, and 36 torsion modes. The detailed potential energy distribution, as well as the scaled and unscaled vibrational assignments, are presented in Table 2. The theoretical IR intensity and Raman spectra can be seen in Fig. 1.

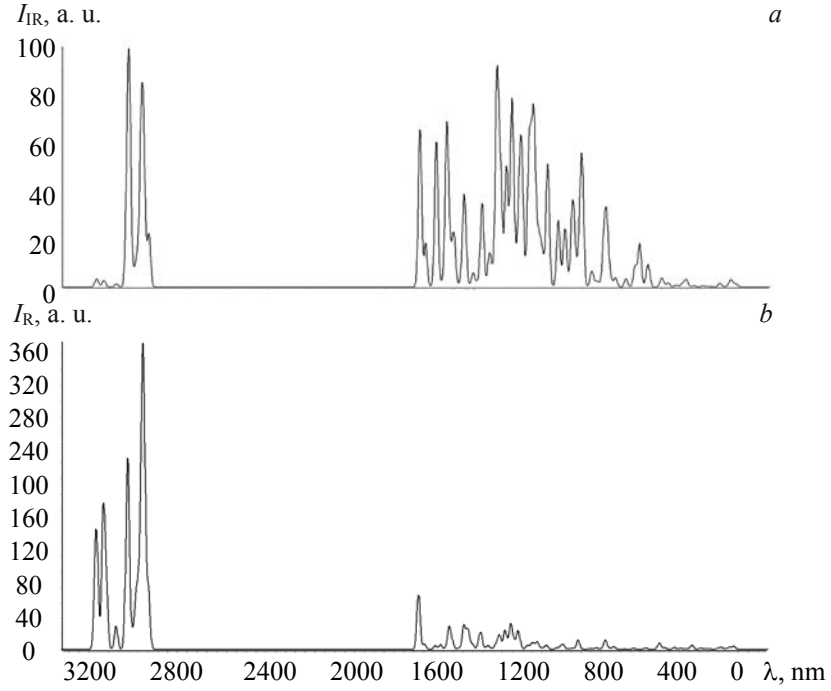

Fig. 1. The theoretical Infrared (a) and Raman (b) spectra of propiconazole.

TABLE 2. Detailed Assignments of Theoretical Wavenumbers (cm^{-1}) of Propiconazole Along with %PED

DFT/B3LYP/ aug-cc-pVDZ	Scaled	*I*(IR)	*I*(R)	Assignment (%PED)
3269	3172	0.94	65.56	$\nu_{(CH)}$99
3260	3164	3.19	114.65	$\nu_{(CH)}$99
3227	3131	1.60	154.55	$\nu_{(CH)}$100
3225	3130	1.40	25.48	$\nu_{(CH)}$93
3210	3115	0.15	67.07	$\nu_{(CH)}$93
3162	3068	1.39	30.46	$\nu_{(CH)}$98
3109	3017	30.95	87.27	$\nu_{(CH))}$86
3102	3010	33.71	88.43	$\nu_{(CH)}$97
3101	3009	8.63	82.25	$\nu_{(CH)}$99
3096	3004	55.56	17.54	$\nu_{(CH)}$74
3075	2984	5.53	21.49	$\nu_{(CH)}$68

Continue Table 2

DFT/B3LYP/ aug-cc-pVDZ	Scaled	*I*(IR)	*I*(R)	Assignment (%PED)
3058	2967	12.17	71.62	$\nu_{(CH)}64$
3038	2948	57.98	129.19	$\nu_{(CH)}83$
3027	2937	45.23	39.3	$\nu_{(CH)}79$
3025	2935	15.43	259.18	$\nu_{(CH)}65$
3017	2928	5.87	88.84	$\nu_{(CH)}63$
2998	2909	24.15	75.73	$\nu_{(CH)}98$
1625	1577	73.05	70.97	$\nu_{(CC)}65$
1595	1548	20.27	6.83	$\nu_{(CC)}63+\delta_{(HCC)}21$
1540	1494	67.78	4.75	$\nu_{(NC)}58+\delta_{(HCN)}27$
1513	1468	2.08	6.16	$\delta_{(HCH)}69$
1487	1443	35.36	0.17	$\delta_{(HCC)}39+\delta_{(HCH)}58$
1477	1433	6.90	5.04	$\delta_{(HCH)}72+\tau_{(HCCC)}15$
1470	1426	1.69	6.49	$\delta_{(HCH)}52+\tau_{(HCCC)}13$
1468	1425	8.94	17.64	$\nu_{(NC)}31+\delta_{(HCN)}10$
1457	1414	1.48	7.15	$\delta_{(HCH)}74$
1451	1408	22.73	2.92	$\delta_{(HCN)}21+\delta_{(HCH)}20+\nu_{(NC)}13$
1421	1379	1.41	1.68	$\tau_{(HCOC)}39$
1402	1361	29.47	2.20	$\nu_{(CC)}36+\delta_{(HCC)}20$
1396	1355	2.35	0.05	$\delta_{(HCH)}87$
1394	1353	14.89	29.13	$\nu_{(NC)}53+\delta_{(HCN)}13$
1381	1340	0.38	1.42	$\tau_{(HCOC)}31+\tau_{(HCCC)}13$
1374	1333	0.01	23.79	$\tau_{(HCCC)}57$
1356	1316	3.89	4.17	$\delta_{(HCO)}60$
1351	1311	2.67	3.23	$\nu_{(NC)}15+\delta_{(HCN)}25$
1335	1295	1.45	0.72	$\tau_{(HCOC)}18$
1320	1281	2.21	2.35	$\nu_{(CC)}81$
1315	1276	0.83	4.95	$\delta_{(HCC)}64$
1308	1269	37.44	17.88	$\delta_{(NCN)}48+\delta_{(HCN)}20+\nu_{(NC)}14$
1278	1240	0.94	1.65	$\tau_{(HCOC)}31$
1271	1233	13.56	4.03	$\delta_{(HCC)}71$
1258	1221	5.59	0.83	$\delta_{(HCC)}39$
1234	1197	88.36	5.50	$\delta_{(HCO)}15+\delta_{(HCN)}14$
1225	1189	14.56	1.35	$\delta_{(HCN)}38+\delta_{(NCN)}13$
1215	1179	4.92	14.26	$\nu_{(CC)}13+\delta_{(HCO)}30$
1209	1173	5.81	4.61	$\nu_{(NC)}10+\delta_{(HCN)}13$
1185	1150	55.14	24.92	$\tau_{(HCOC)}10$
1161	1127	24.72	12.30	$\delta_{(HCN)}41+\delta_{(CNN)}33+\delta_{(CNN)}33$
1157	1123	43.58	6.70	$\delta_{(HCC)}21$
1153	1119	21.67	16.00	$\delta_{(HCC)}31$
1140	1106	0.26	8.38	—
1119	1086	41.93	23.36	$\nu_{(CC)}41+\nu_{(ClC)}14+\delta_{(HCC)}11$
1107	1074	50.29	2.91	$\nu_{(CC)}10$
1073	1041	29.59	2.82	$\delta_{(HCC)}13+\delta_{(CCC)}15$
1071	1039	20.40	1.76	$\nu_{(CC)}34$
1060	1029	41.43	1.85	$\nu_{(OC)}14++\nu_{(NC)}15$
1046	1015	68.77	7.76	$\nu_{(CC)}34+\nu_{(OC)}28$
1032	1001	11.28	2.62	$\nu_{(OC)}15$
1021	991	18.19	8.85	$\nu_{(NC)}35$
1005	975	16.06	1.52	$\tau_{(HCOC)}13$
986	957	5.28	1.34	$\tau_{(HCCC)}67$

Continue Table 2

DFT/B3LYP/ aug-cc-pVDZ	Scaled	*I*(IR)	*I*(R)	Assignment (%PED)
976	947	53.39	4.01	$\delta_{(CCC)}22$
969	940	1.14	1.24	$\delta_{(NCN)}63+\nu_{(NN)}10$
923	896	30.59	2.45	$\nu_{(OC)}26+\delta_{(OCC)}13$
900	873	0.21	4.15	$\nu_{(CC)}41+\tau_{(HCCC)}17$
895	869	7.69	0.28	$\tau_{(HCNN)}82+\tau_{(CNNC)}12$
887	861	10.07	4.24	$\delta_{(HCC)}14+\tau_{(HCCC)}23$
886	860	11.64	0.05	$\tau_{(HCCC)}69+\gamma_{(ClCCC)}12$
856	831	8.14	0.59	$\tau_{(HCNC)}66+\tau_{(CNNC)}12$
849	824	30.12	0.51	$\tau_{(HCCC)}14+\nu_{(OC)}10$
838	813	11.87	0.61	$\tau_{(HCCC)}50$
815	791	19.29	12.24	$\nu_{(OC)}28+\nu_{(ClC)}14$
802	778	54.25	1.15	$\delta_{(CCC)}21+\nu_{(ClC)}21$
753	731	7.15	1.10	$\tau_{(CCCC)}12$
736	714	1.36	0.26	$\tau_{(HCCC)}44+\delta_{(HCC)}10$
722	701	2.30	1.91	$\tau_{(CCCC)}22$
692	672	20.38	0.37	$\tau_{(CNNC)}59+\tau_{(HCNN)}16+\tau_{(NCNN)}15$
679	659	19.91	3.92	$\delta_{(CCC)}16+\tau_{(NCNN)}15$
675	655	10.79	8.63	$\delta_{(CCC)}54$
659	639	4.61	1.80	$\tau_{(NCNN)}18+\delta_{(CCC)}10+\delta_{(OCC)}16$
633	614	4.35	3.86	$\tau_{(CNNC)}10+\tau_{(NCNN)}21$
580	563	3.82	0.40	$\tau_{(ClCCC)}44+\tau_{(CCCC)}16+\tau_{(HCCC)}12$
534	518	9.48	1.48	$\tau_{(OCCC)}12+\delta_{(CCC)}13$
511	496	20.00	0.06	$\delta_{(CCC)}14+\delta_{(ClCC)}12+\nu_{(ClC)}12+\nu_{(CC)}12$
472	458	5.41	1.69	$\nu_{(ClC)}12+\gamma_{(ClCCC)}24$
465	451	6.17	0.29	$\tau_{(CCCC)}36+\tau_{(HCCC)}19+\gamma_{(ClCCC)}17$
402	390	1.83	6.77	$\nu_{(ClC)}39$
395	383	2.75	2.11	$\delta_{(OCC)}11+\delta_{(ClCC)}18+\tau_{(OCCC)}10$
375	364	0.32	1.69	$\delta_{(NCC)}11+\delta_{(CCC)}10+\tau_{(CCCC)}12+\gamma_{(ClCCC)}12$
365	354	1.80	0.46	$\delta_{(CNN)}21$
326	316	0.91	2.77	$\delta_{(CCC)}19+\delta_{(ClCC)}10$
297	288	0.94	1.08	$\gamma_{(OCCC)}22$
289	280	0.78	0.38	$\delta_{(CNN)}20+\delta_{(OCC)}23+\delta_{(CCC)}11$
274	266	3.40	0.73	$\delta_{(CCN)}27+\tau_{(OCCC)}12+\tau_{(CCNN)}16$
249	242	0.08	0.49	$\tau_{(HCCC)}64$
235	228	0.60	5.56	$\delta_{(CCC)}16+\nu_{(CC)}16$
194	188	0.39	1.42	$\delta_{(ClCC)}70$
185	180	0.30	0.16	$\tau_{(HCOC)}22+\delta_{(CCC)}25+\delta_{(CCO)}15$
173	168	0.04	0.79	$\tau_{(CCCC)}21+\gamma_{(ClCCC)}50$
162	157	0.24	0.33	$\delta_{(CCC)}30$
145	141	0.08	0.67	$\delta_{(CCC)}24+\gamma_{(CCNN)}10$
105	102	1.75	1.11	$\gamma_{(CCNN)}26+\delta_{(CCN)}10$
90	87	0.09	2.48	$\tau_{(CCCC)}22+\gamma_{(CCNC)}25$
77	75	0.11	0.65	$\tau_{(CCNC)}46$
61	59	0.34	0.67	$\tau_{(COCC)}12+\tau_{(CCNC)}24$
50	49	2.38	0.80	$\tau_{(CCCC)}12+\tau_{(CCNC)}40+\tau_{(COCC)}13$
45	44	0.53	1.61	$\tau_{(CCCC)}35+\tau_{(CCNC)}16$
39	38	0.92	0.25	$\tau_{(COCC)}15+\tau_{(CCCN)}19$
26	25	0.41	2.60	$\tau_{(CCCC)}28+\tau_{(CCCN)}33$
20	19	0.96	1.79	$\tau_{(CCCN)}20+\tau_{(COCC)}37+\delta_{(OCC)}11$

Both IR and Raman vibrational spectroscopy techniques complement each other. Weak bands in the IR spectrum appear as strong bands in the Raman spectrum, and vice versa. This relationship is clearly observed in Table 2 and Fig. 1. The most prominent bands in the Raman spectrum correspond to the C-H stretching vibrations at 3131, 2948, and 2935 cm^{-1}. These vibrational bands appear as medium and weak bands in the IR spectrum. On the other hand, the strongest bands in the fingerprint region of the IR spectrum are N-C at 1494 cm^{-1}, H-C-O at 1197 cm^{-1}, C-C at 1074 and 1015 cm^{-1}, and C-C-C at 947 and 778 cm^{-1}. In the Raman spectrum, these bands are observed as weak bands.

The calculated C-H stretching frequencies are as follows: 3172, 3164, 3131, 3130, 3115, 3068, 3017, 3010, 3009, 3004, 2984, 2967, 2948, 2937, 2935, 2928, and 2909 cm^{-1}. The corresponding potential energy distribution (%PED) contributions are 99, 99, 100, 93, 93, 98, 86, 97, 99, 74, 68, 64, 83, 79, 65, 63, and 98%, respectively. Among these vibrational bands, those observed in the range of 3172–3068 cm^{-1} correspond to the C-H symmetric and asymmetric vibration bands of the benzene and pyrrole ring, while those observed in the 3017–2909 cm^{-1} region correspond to the C-H symmetric and asymmetric vibration bands of the CH2 and CH3 groups.

The calculated C-C stretching frequencies are as follows: 1577, 1548, 1361, 1281, 1086, 1074, 1039, and 873 cm^{-1}. The corresponding PED contributions are 65, 63, 36, 81, 41, 10, 34, and 41%, respectively. Upon examining the PED distributions, it can be observed that the H-C-C bending vibration (δHCC), H-C-C-C torsion vibration (τHCCC), and O-C stretching vibration (νOC) contribute to the C-C stretching vibrations.

The vibrational bands related to the C-X (X = Cl, Br, I) group can be assigned in the frequency region of 1129–480 cm^{-1} [19, 20]. In this study, the C-Cl stretching vibration (νClC) bands were calculated at 778 and 390 cm^{-1}, the Cl-C-C bending (δClCC) bands at 383 and 188 cm^{-1}, and the Cl-C-C-C out-of-plane bending vibration (γClCCC) bands at 860, 458, and 168 cm^{-1}. The PED contributions for these vibration bands are 21, 39, 18, 70, 12, 24, and 50%, respectively.

The C-O stretching vibration is observed in the region of 1260–1000 cm^{-1} in the spectrum. The C-O stretching mode can be combined with the C-C stretching vibration, resulting in an asymmetric C-C-O stretching vibration [21]. In this study, the C-O stretching vibration bands were observed at 1029 and 1001 cm^{-1}, while the O-C stretching and C-C-O bending vibration bands were observed together at 896 cm^{-1}. These bands appeared as medium bands in the IR spectrum but were observed as weak bands in the Raman spectrum.

Other characteristic vibration bands of propiconazole include the C-N, N-C-N and N-N bands. In this study, C-N stretching vibrations were observed along with H-C-N bending vibration bands at 1494, 1353, and 1311 cm^{-1}. The PED ratios for the C-N and H-C-N vibration bands were calculated as 58–27, 53–13, and 15–25%, respectively. N-C-N bending vibrations were observed in conjunction with H-C-N bending vibrations at 1269, 1189, and 1127 cm^{-1}. The PED contributions to these vibration bands were calculated as 48–20, 13–38, and 33–41%, respectively.

The MEP surface provides valuable information about the charge distribution and variable charge regions of molecules [22, 23–26]. Charge distribution is a commonly used method for predicting intermolecular interactions, molecular behavior, structural activity, and both electrophilic and nucleophilic reactivity. It also plays a role in detailing hydrogen bonding [23]. MEP is closely related to the chemical behavior, dipole moment, and electronegativity of a molecule [24].

Figure 2 presents a color-coded representation of the electrostatic potential surface. The potency decreases in the order of blue > green > yellow > orange > red. In the MEP surface, the electron-deficient region is indicated by the blue color, the electron-rich region is represented by the red color, and the neutral zero electrostatic potential region, which indicates hydrogen-bond interactions, is shown in green [25]. The positive MEP corresponds to the repulsion of the proton/cation in the blue region, caused by the atomic nucleus. On the other hand, the negative MEP represents the attraction of a proton/light cation in the red region due to the concentrated electron density in the molecule [24].

For propiconazole, the scaling order ranges from −1.52 eV (red, indicating the strongest attraction) to 1.52 eV (blue, indicating the strongest repulsion). The MEP surface reveals that the negative potential sites are located on the nitrogen atoms, making them the most favorable regions for nucleophilic attacks. Additionally, the maximum positive region is localized on the hydrogen atoms in the carbonyl and amine groups, suggesting a potential site for electrophilic attack. Atomic charge in a molecule is a fundamental chemical property that proves useful in explaining charge transfer mechanisms and electronic structures in chemical reactions [26]. In Akman's study, it was demonstrated that the positive regions in the MEP map of the N-iso-

propylmethacrylamide molecule are located above the N-H groups, while the negative regions are positioned above the C=O groups. Furthermore, the reactive regions were observed around the hydrogen atoms [26].

Mulliken population analysis, widely used for determining atomic charge information in molecules, is well-defined from a quantum mechanical perspective. Marinho et al. conducted a study on Topiroxostat, where they utilized Mulliken population analysis to investigate charge variations among different atoms [27]. Figure 3 presents the Mulliken charges of the molecules under investigation. Analysis of the Mulliken charge distribution revealed significant variations, with the highest variation observed among carbon atoms, followed by nitrogen and hydrogen atoms. Carbon atoms exhibited a range of +1.81 to –0.35, while hydrogen atoms displayed 10 different charge values. Specifically, carbon atoms C15 and C21, which are bonded to chlorine atoms, carried negative charges, while other carbon atoms were positively charged. The oxygen atoms, O3 and O4, were found to have Mulliken charges of –0.76 and –0.79, respectively. Similarly, the Mulliken charges for Cl1 and Cl2 were –0.30 and –0.22, respectively. Due to their higher electronegativity, all oxygen and nitrogen atoms exhibited negative Mulliken charges.

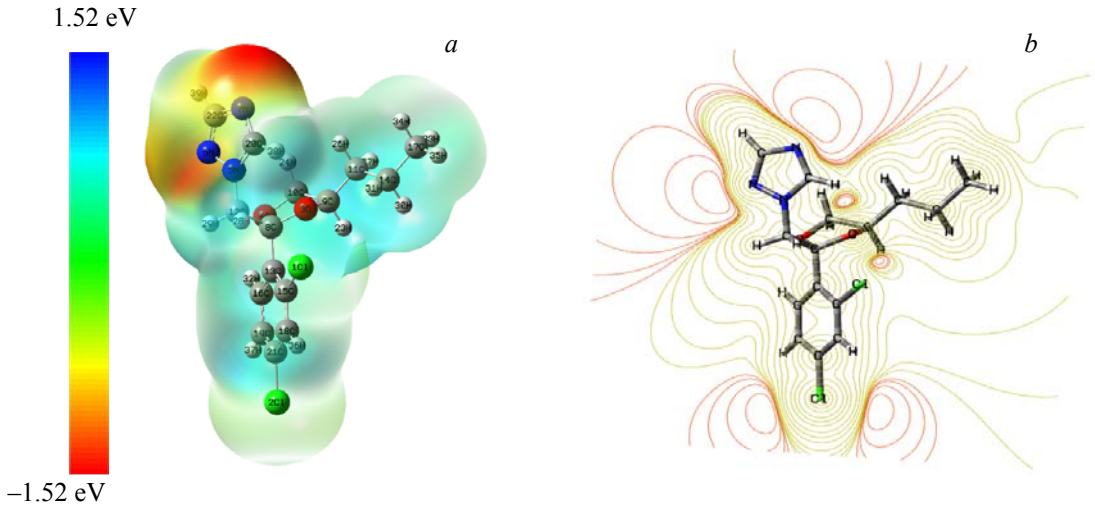

Fig. 2. (a) Molecular electrostatic potential map, (b) visualization for the mapping of total density of propiconazole.

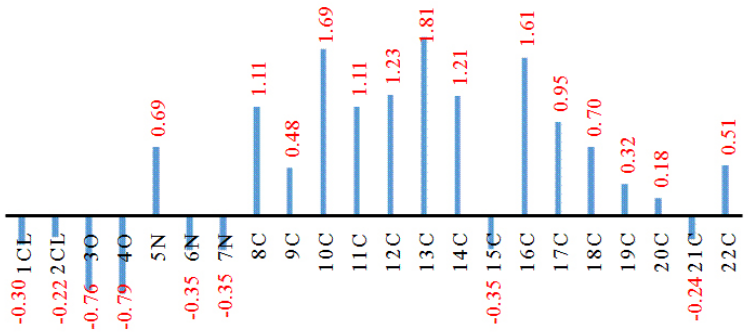

Fig. 3. Mulliken atomic charge of propiconazole.

Frontier molecular orbitals (FMOs), consisting of the highest occupied molecular orbitals (HOMOs) and the lowest unoccupied molecular orbitals (LUMOs), are essential descriptors in quantum mechanics that play a crucial role in determining chemical interactions. FMO analysis is widely employed to explore various properties of chemical structures, including molecular electrical transport, conductivity, biological properties, chemical reactivity, and kinetic stability. The energy gap between the HOMO and LUMO, known as the HOMO-LUMO energy gap, serves as a key determinant of a molecule's kinetic stability, chemical reactivity, optical polarizability, and chemical hardness-softness. A large HOMO-LUMO energy gap indicates a “hard” molecule that requires substantial energy for excitation. Conversely, a small HOMO-LUMO energy gap characterizes a “soft” molecule, which exhibits low kinetic stability but high polarizability and chemical activity. The energy gap significantly influences the chemical and spectroscopic properties of a structure.

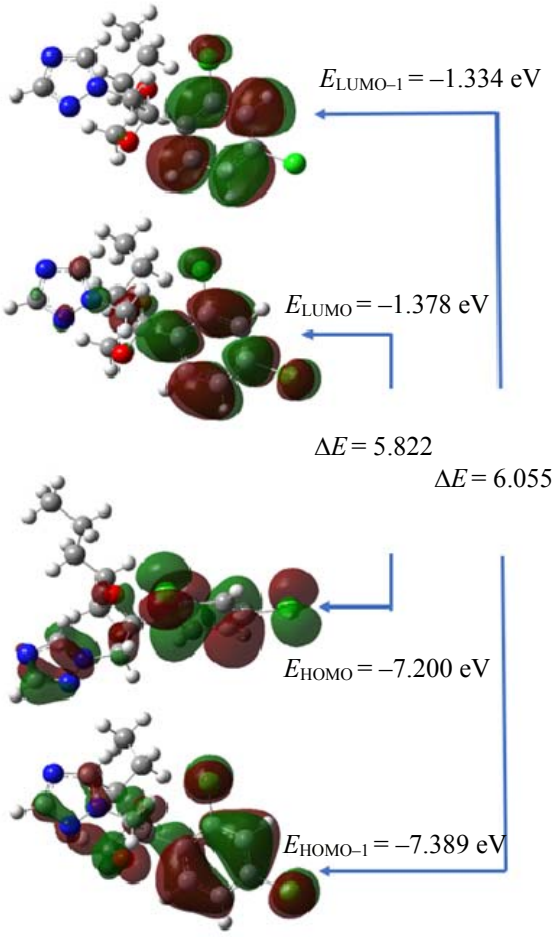

Fig. 4. HOMO and LUMO plot of propiconazole.

In this study, FMO analysis was performed using the B3LYP/aug-cc-pVDZ basis set in DFT mode. Table 3 presents the mathematical formulas and data for the quantum chemical properties, determined based on the HOMO and LUMO energies. Figure 4 illustrates the distribution of HOMO and LUMO orbitals in the ground state. The formation of HOMO orbitals involves contributions from O4, Cl1, Cl2 atoms, and C-N, C-C, C-H, and C-O bonds, while C22, O3, O4, C12, N5, N6 atoms, and C-C, C-H bonds contribute to the formation of LUMO orbitals. The calculated HOMO and LUMO energies for the propiconazole molecule were –7.200 and –1.378 eV, respectively, resulting in a band gap of 5.822 eV. The electrophilicity index (w) is employed to gain insights into the reactivity, structure, and dynamics of a molecule. Organic molecules with a $w > 1.5$ eV are considered strong electrophiles. For the propiconazole molecule, the w value was determined as 3.160 eV, indicating its electrophilic nature. A negative chemical potential (μ) value signifies the stability of a molecule, suggesting that it will not readily decompose into its constituent elements. The calculated μ value for this molecule was –4.289 eV.

Molecular docking simulations were conducted to elucidate the mechanism and modes of interaction between the propiconazole pesticide and DNA. The crystal structure of DNA (PDB ID: 1BNA) was obtained from the protein database [28]. The docking study of the propiconazole molecule was performed using AutoDock Vina [16], Autodock Tools, and PyMOL Molecular Graphics System [17] programs. Many macromolecular structure data in PDB files do not include hydrogen atoms, and the ionization state of protein residues is often uncertain, necessitating their inclusion in the optimization process. Therefore, charges and hydrogen atoms were added to enable proper optimization. To prepare DNA for the insertion study, water molecules were removed, and polar hydrogens were added. Kollman's DNA charges were calculated prior to the insertion study.

TABLE 3. Global Chemical Reactivity Indices for the Propiconazole

Parameter	Value, eV
E_{HOMO}	–7.200
E_{LUMO}	–1.378
ΔE	5.822
Ionization potential ($I = -E_{HOMO}$)	7.200
Electron affinity ($A = -E_{LUMO}$)	1.378
Electronegativity ($\chi = (I+A)/2$)	4.289
Chemical potential ($\mu = -(I+A)/2$)	–4.289
Chemical hardness ($\eta = (I-A)/2$)	2.911
Chemical softness ($s = 1/2\eta$)	0.170
Electrophilic index ($w = \mu^2/2\eta$)	3.160

Figure 5 displays the 3D molecular structure of the propiconazole molecule bound to DNA. Gas phase calculations revealed that the most stable conformer of propiconazole formed hydrogen bonds and van der Waals forces with deoxyadenosine5 (DA5), deoxyadenosine6 (DA6), deoxycytosine21 (DC21), deoxycytosine23 (DC23), deoxyguanine4 (DG4), deoxyguanine22 (DG22), and deoxythymine7 (DT7) nucleic acids (Fig. 5). The DNA binding affinity (ΔGbind) of propiconazole was determined to be -6.6 kcal/mol. The interactions between propiconazole and nucleic acids are as follows:

Interaction with DT7: Hydrogen bond with a length of 3.55 Å.

Interaction with DG4: Hydrogen bonds with lengths of 2.7 and 2.4 Å.

Interaction with DG22: Hydrogen bonds with lengths of 2.9, 3.55, and 3.22 Å.

Van der Waals forces were observed between DNA residues (DA5, DA6, DC21, and DC23) and the propiconazole molecule. Importantly, the molecular regions associated with these interactions correspond to those previously observed in the MEP analyzed above.

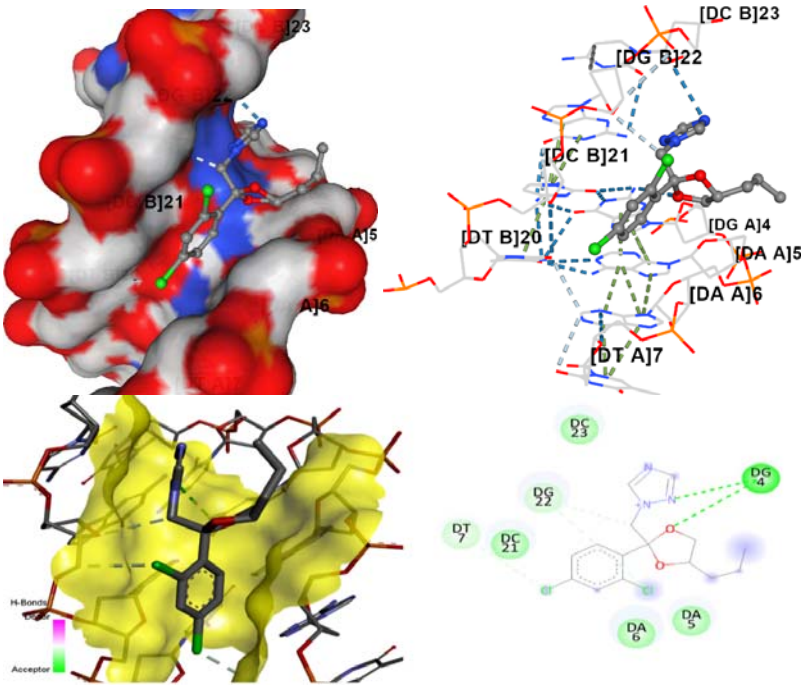

Fig. 5. Docking of propiconazole with DNA.

Zhang et al. [29] highlighted hydrogen bonds as the predominant factor contributing to the specific bonding between pesticide molecules and DNA bases in their study on the interaction of triadimenol and DNA. Corregidor et al. [30] investigated the DNA interaction of flonicamid (a pesticide) and identified six hydrogen bonds: G10 (2.91 Å), C9 (3.00 Å), G16 (2.99 Å), A17 (2.15 Å), and A18 (2.33 and 3.10 Å). Ahmad et al. [31] studied the DNA binding properties of the herbicide pendimethalin and found that it can bind

to the G-C-rich region of DNA. Çelik et al. [32] conducted a molecular docking study on cyclo(Ala-His)-DNA and demonstrated peptide-nucleic acid interactions through hydrogen bonding interactions with DC9 (3.1 Å), DG10 (2.39 Å), DC11 (2.96 Å), DG16 (2.53 Å), and DA17 (2.39 and 2.99 Å). The comparative data from the literature, along with the results of this study, support the existence of interactions between propiconazole pesticides and DNA.

Furthermore, after the molecular docking analysis, changes in bond lengths between atoms were observed in the region where the propiconazole molecule interacts with DNA – for example, the bond length between Cl2 and C21 atoms of optimized propiconazole was 1.72 Å, which increased to 1.76 Å after molecular docking analysis. A similar change in bond length was observed between Cl1 and C15 atoms, which increased from 1.73 to 1.77 Å. The same trend was observed for the nitrogen atom involved in the interaction. The bond length between N5 and N6 atoms was 1.33 Å before molecular docking, which increased to 1.36 Å after molecular docking.

Conclusions. The present study aimed to provide a comprehensive theoretical characterization of the propiconazole pesticide using spectroscopic techniques and to predict its interaction with DNA through molecular docking analysis. The fungicide propiconazole was subjected to various analyses, including structural details, vibrations, electrostatic potential, Mulliken population, HOMO-LUMO, and thermodynamic analyses, using DFT calculations.

The HOMO-LUMO energy range indicated that the compound is reactive and polarizable, suggesting its potential for chemical reactivity and optical polarizability. The molecular electrostatic potentials and electrostatic potential surfaces revealed that the N6 and N7 atoms exhibited negative potential, making them susceptible to nucleophilic attacks. Similar reactivity patterns were observed for oxygen and chlorine atoms. Molecular docking analysis further supported the preferential binding of propiconazole to DNA, particularly in regions rich in G-C base pairs.

These findings provide insights into the mechanism of DNA damage and the potential toxicological effects of the pesticide. Moreover, this knowledge can contribute to the development of new pesticides with reduced toxicity. When combined with existing literature, these results emphasize the importance of careful consideration and regulation regarding the widespread use of pesticides.

The comprehensive characterization and molecular docking analysis of propiconazole pesticide shed light on its reactivity, potential interactions with DNA, and implications for toxicity. These findings serve as a valuable resource for designing safer pesticides and raising awareness about the need for responsible pesticide usage.

REFERENCES

1. X. Tan, Z. Wang, D. Chen, K. Luo, X. Xiong, Z. Song, *Chemosphere*, **108**, 26–32 (2014).
2. Y. Zhang, G. Zhang, Y. Li, Y. Hu, *J. Agric. Food Chem.,* **61**, No. 11, 2638−2647 (2013).
3. C. Wang, Y. Li, *J. Agric. Food Chem*., **59**, No. 15, 8507–8512 (2011).
4. E. Kurti, D. Heyd, S. Wylie, *Wood Sci. Technol.*, **39**, 618–629 (2005).
5. N. O. Costa, M. L. Vieira, V. Sgarioni, M. R. Pereira, B. G. Montagnini, S. D. F. P. Mesquita, D. C. C. Gerardin, *Toxicology*, **335**, 55–61 (2015).
6. P. J. Chen, T. Moore, S. Nesnow, *Toxicol. in Vitro*., **6**, No. 22, 1476–1483 (2008).
7. A. A. Khalaf, M. Elhady, E. Hassanen, A. Azouz, M. Ibrahim, M. Galal, P. Noshyve, R. Azouz, *Rev. Bras. Farm*., **31**, 67–74 (2021).
8. X. Pan, Y. Cheng, F. Dong, N. Liu, J. Xu, X. Liu, X. Wu, Y. Zheng, *J. Hazard. Mater.*, **359**, 194–202 (2018).
9. H. C. Kwon, H. Sohn, D. H. Kim, D. M. Shin, C. H. Jeong, Y. H. Chang, J. H. Yune, Y. J. Kim, S. H. Kim, S. G. Han, *J. Agric. Food. Chem*., **69**, No. 26, 7399–7408 (2021).
10. F. Ekelund, K. Westergaard, D. Soe, *Biol. Fertil. Soils*., **31**, 70–77 (2000).
11. S. Kurth, M. Marques, E. Gross, *Cond. Matter Phys*., 395–402 (**2005**).
12. N. Rezki, F. Faleh Al-blewi, S. Al-Sodies, A. Khalid Alnuzha, M. Messali, I. Ali, M. Reda Aouad, *ACS Omega*, **5**, No. 10, 4807–4815 (2020).
13. M. Frisch, G. Trucks, G. Schlegel, M. Suzerain, M. Robb, J. Cheeseman, J. Montgomery, T. Vreven, K. Kudin, J. Burant, J. Millam, S. Iyengar, J. Tomasi, V. Barone, B. Mennucci, M. Cossi, G. Scalmani, N. Rega, G. Petersson, H. Nakat, *Gaussian 09* (2003).
14. R. Dennington, T. Keith, *Gausswiev 5* (2009).

15. M. Jamroz, *Vibration Energy Distribution Analysis VEDA* (2004).
16. W. Lindstrom, *Using AutuDock 4 for Virtual Screening* (2008).
17. L. Schrodinger, *The PyMOL Molecular Graphics System, Version 2.4.1*, Schrodinger (2015).
18. L. Jin-xiang, Y. Chun-long, *Chin. J. Pesticide Sci*., **8**, No. 1, 20–24 (2006).
19. S. Premkumar, A. Jawahar, T. Mathavan, M. Kumara Dhas, V. Sathe, A. Milton Franklin Benial, *Spectrochim. Acta A: Mol. Biomol. Spectrosc*., **129**, 74–83 (2014).
20. K. Saraswathi, M. Suresh, A. Pandurangan, *J. Mol. Struct*., **1255**, 132447 (2022).
21. R. Silverstein, F. Webster, D. Kiemle, *Spectrometric Identification of Organic Compounds*, 7 ed., John Wiley& Sons (2005).
22. N. Kaya Kınaytürk, T. Kalaycı, B. Tunalı, *Spectrosc. Lett.*, **54**, No. 9, 1–15 (2021).
23. F. Berrah, F. Boursas, S. Bouacida, F. Ouannassi, *J. Mol. Struct.*, **1205**, 127624 (2020).
24. J. S. Singh, M. S. Khan, S. Uddin, *Polym. Bull.*, **80**, 3055–3083 (2023).
25. M. E. Moghadam, A. Jafari, R. K. Khashandaragh, A. Divsalar, M. Ghasemzadeh, *J. Iran. Chem. Soc*., **18**, 1927–1939 (2021).
26. F. Akman, *Russ. J. Phys. Chem. B*, **15**, No. 3, 517–532 (2021).
27. E. S. Marinho, M. M. Marinho, *Int. J. Sci. Eng. Res*., **7**, No. 8, 1264–1270 (2016).
28. https://www.rcsb.org/structure/1BNA (accessed: 10 April 2022).
29. Y. Zhang, G. Zhang, P. Fu, Y. Ma, J. Zhou, *Spectrochim. Acta A: Mol. Biomol. Spectrosc.*, **96**, 1012–1019 (2012).
30. P. F. Corregidor, M. Zigolo, E. Ottavianelli, *J. Mol. Struct*., **1241**, 130628 (2021).
31. I. Ahmad, A. Ahmad, M. Ahmad, *Phys. Chem. Chem. Phys*., **9** (2016).
32. S. Celik, G. Yilmaz, A. Ozel, S. Akyuz, *J. Biomol. Struct. Dyn.*, **40**, No. 2, 660–672 (2022).